RSC Advances

PAPER

View Article Online
View Journal | View Issue

Cite this: *RSC Adv.*, 2025, **15**, 38158

Doping effect of antimony on $BaFeO_3$ perovskite oxide: optical, electronic, magnetic and thermoelectric properties

Md. Riad Khan,[a] Sanzida Naznin Mim,[a] Zihad Hossain,[a] Md. Emon Hassan,[a] Md. Saiful Alam,[b] Mohammad Abdur Rashid[c] and Md. Lokman Ali *[a]

Perovskite oxides have attracted significant attention in contemporary research due to their tunable properties achieved through doping. The concerns of toxicity with lead (Pb)-doped perovskites highlight the need for environmentally friendlier alternatives such as antimony (Sb)-doped perovskites. In this study, the electronic, magnetic, structural, optical and thermoelectric properties of Sb-doped $BaFeO_3$ (BFO) are investigated using the full-potential linearized augmented plane wave (FP-LAPW) method based on density functional theory (DFT) in conjunction with the Boltzmann transport theory. The doping levels considered are $x = 0.125$ and 0.25 for the composition of $BaFe_{1-x}Sb_xO_3$. The DFT simulations reveal that Sb doping on BFO causes a slight lattice distortion but retains the cubic structure (space group 221-$Pm\bar{3}m$), indicating the material's structural stability. The density of states at the Fermi level (E_F) increased with Sb doping, indicating an enhanced carrier concentration. The computed optical characteristics reveal that pure BFO has strong ultraviolet absorption. In contrast, $BaFe_{0.875}Sb_{0.125}O_3$ (12.5% Sb-doped BFO) and $BaFe_{0.75}Sb_{0.25}O_3$ (25% Sb-doped BFO) show a progressive reduction with Sb substitutional doping, accompanied by a significant drop in the extinction coefficient and dielectric constant. The plasma frequency decreased from 3.372 eV (pure BFO) to 1.0548 eV (25% Sb-doped), indicating a reduction in free-carrier activity and metallic characteristics. The computed figure of merit ($ZT \approx 0.50$) shows significant enhancement after 25% Sb doping. In addition, this study highlights that Sb doping on BFO greatly improves the dual tunability of optical transparency and thermoelectric efficiency through substitutional doping.

Received 18th August 2025
Accepted 25th September 2025

DOI: 10.1039/d5ra06101f

rsc.li/rsc-advances

1. Introduction

In today's scientific era, perovskite oxides with the general formula ABO_3 (where A = larger cation and B = smaller cation) have received widespread attention due to their versatile, tuneable properties.[1–3] They offer potential applications in various fields because of their adjustable characteristics, multiferroic nature, photo-catalytic activity, bio-compatibility and energy harvesting capability.[4–7] These materials are widely studied due to their structural flexibility and stability, which allow for various cation substitutions, leading to tunable properties that can be optimized for specific applications such as fuel cells, gas sensors, superconductors, and memory devices.[8] In the last few years, perovskite-type oxides, such as $ATiO_3$ (where A = Mn, Fe, Co, Ni and Ba),[9–13] $LaMnO_3$,[14] $SrTiO_3$,[15] $LaAlO_3$,[16] and WBO_3 (where B=Cr, Hg),[17] have been exclusively investigated for their potential applications. The growing interest in these materials emerges from their exceptional versatility in electronic structure, phase transitions and defect chemistry, making them ideal candidates for advanced technologies like artificial photosynthesis, transparent conducting oxides and thermoelectric energy conversion.[18,19] Among them, nickel titanate ($NiTiO_3$) is one of the perovskite materials with remarkable photocatalytic properties for the evolution of hydrogen and the degradation of harmful substances.[20] However, one of the most significant categories within the perovskite family is Fe-based perovskites $AFeO_3$ (where A = Sr, La, Bi, and Ba).[21–24] These materials exhibit fascinating properties, such as colossal magnetoresistance, high-temperature waste heat recovery systems, high thermal stability and excellent electrical conductivity, making them suitable for catalytic, spintronic, and electronic applications.[18,25–27] The tunability of their conductivity, absorptivity, reflectivity, and dielectric and thermoelectric properties has made them attractive candidates for photovoltaic and thermoelectric applications.[28] Recently, metallic barium ferrite $BaFeO_3$ (BFO), a rare member of the perovskite oxide family, is given immense focus for its photovoltaic and thermoelectric applications.[29] BFO is distinguished

[a]Department of Physics, Pabna University of Science and Technology, Pabna-6600, Bangladesh. E-mail: lokman.cu12@gmail.com
[b]Department of Physics, University of Chittagong, Hathazari-4331, Bangladesh
[c]Department of Physics, Jashore University of Science and Technology, Jashore-7408, Bangladesh

by its strong magnetic ordering, high electrical conductivity, and cubic symmetry, all of which are based on the mixed valence states of iron (Fe^{3+}/Fe^{4+}) and strong Fe–O–Fe super exchange interactions.[30] Unlike the majority of other transition metal perovskites, it is metallic due to the double exchange process that promotes delocalized electron transport across the Fe–O–Fe framework.[31] Because of these characteristics, BFO has drawn a lot of interest for applications in magnetic sensors, spintronics, and next-generation electronic devices, where magnetic control and quick charge transport are crucial.[32] Furthermore, its high hybridization between Fe-3d and O-2p orbitals promotes outstanding electrical mobility, while its structural plasticity allows for various forms of cationic replacement without damaging the perovskite framework. As a result, BFO is both scientifically and technologically fascinating, particularly in applications such as medium-temperature waste heat recovery systems, IR filter coatings, magneto-electronics, waste water recovery and high-temperature magnetic switches.[33–36] Recent studies have focused on enhancing the functionalities of BFO to meet the demands of contemporary applications by introducing dopants. Doping is one of the best methods for adjusting the characteristics of perovskite oxides, like BFO, where foreign atoms are intentionally incorporated into the material's crystal lattice to fine-tune its structural, optical and electronic properties.[37] Researchers have demonstrated that dopants can induce changes in the oxidation state of the host cation, enhance charge carrier mobility and improve defect chemistry, which are crucial for practical optoelectronic applications, such as photocatalysis, energy harvesting and electronic sensing.[38–40] Therefore, researchers can manipulate the electronic structure, magnetic behavior, optical properties and catalytic activity of the parent material by carefully selecting dopants and regulating their concentration. This opens up new opportunities for the fabrication of advanced devices and photovoltaic and industrial applications.[41] One such promising dopant is Sb, which has the potential to improve the optical absorption and conductivity of BFO, making it an attractive candidate for optoelectronic applications. Sb was selected as a dopant for BFO due to its potential to modify the electronic structure and enhance the material's properties.[42,43] However, the effects of doping on perovskite oxides have been studied extensively; the impact of Sb doping on BFO has not yet been explored in detail using the WIEN2k code based on the full-potential linearized augmented plane wave (FP-LAPW) method. In this study, we explore the exciting topic of Sb doping on BFO and its possible consequences for optoelectronic and thermos-electric applications. Through a comprehensive review of recent literature, we aim to clarify the fundamental principles underlying dopant-induced modifications in BFO and explore their potential for practical applications. Specifically, we strive to dope the Fe-site on BFO with Sb to enhance the optoelectronic performances. Previous studies have suggested that the incorporation of suitable dopants into perovskite oxides can enhance their efficiency and render them promising candidates for optoelectronic applications.[44–46] Our goal is to enhance the material's optoelectronic properties in the visible, IR and UV regions, which are the key parameters for optoelectronic applications. Here, we analyze and discuss the structural, optical, electronic, magnetic and thermo-electric properties of Sb-doped BFO using the FP-LAPW method based on DFT to identify a superior candidate for thermo-electric and optoelectronic applications compared to the previously proposed best lead-free candidate. Some experimental and theoretical works have investigated how doping concentration affects structural, electronic and optical properties. However, to the best of our knowledge, no prior theoretical experiment using Sb doping on perovskite has been conducted using the WIEN2k (18.01) code.[47] This study contributes to the understanding of Sb doping effects by providing insights into the correlation between doping levels and material performance, which can pave the way for designing next-generation perovskite-based devices with enhanced functionalities. This article concludes with a detailed comparison of Sb-doped BFO and pure BFO, focusing on the key parameters that determine the suitability of these materials for practical applications.

2. Computational methods

In this study, first-principles calculations were carried out using the full-potential linearized augmented plane wave (FP-LAPW) method[48] within the WIEN2k simulation package[49] based on DFT. The electronic exchange–correlation effects were treated using the Generalized Gradient Approximation (GGA) as formulated by Perdew, Burke and Ernzerhof (PBE).[50] DFT + U is often applied to BFO to account for strong correlation and covalency effects; the Sb-doped BFO system studied here exhibits metallic behaviour. For such itinerant states, the addition of U may artificially localize delocalized d-electrons, while standard DFT provides a more realistic description of metallic electronic properties.[51] Due to the metallic nature of the BFO under study, all calculations were performed using a spin-polarized approach to account for magnetic interactions. The self-consistent field (SCF) computations were thus executed separately for spin-up and spin-down channels. Structural optimization was performed using the Broyden–Fletcher–Goldfarb–Shanno (BFGS) minimization scheme, with the total energy convergence, force convergence and charge convergence criteria set to 10^{-5} Ry, 1.0 mRy au^{-1} and $10^{-4}e$, respectively. The q-limit is set to 0.02 for SCF with spin polarization calculation. For pure BFO, the wave function cut-off parameter $R_{MT} \times K_{max}$ was set to 7.0, with a cut-off energy of -6.0 Ry, while for the Sb-doped structures, the cut-off energy was increased to -8.0 Ry to account for the larger atomic size and to avoid overlapping muffin-tin spheres. RMT stands for the smallest muffin-tin radius among all atomic spheres. In LAPW-based electronic structure computations, K_{max} and G_{max} are utilised to set the plane wave and Fourier expansion cutoffs. The core and valence electronic configurations used in the calculations included O ($2s^2$ $2p^4$), Fe ($3d^6$ $4s^2$), Ba ($4d^{10}$ $5p^6$ $6s^2$), and Sb ($5s^2$ $4d^{10}$ $5p^3$). The pure BFO crystal adopts a cubic perovskite structure with space group $Pm\bar{3}m$ (no. 221) and contains 5 atoms per unit cell-1 barium (Ba), 1 iron (Fe), and 3 oxygen (O) atoms. A $2 \times 2 \times 2$ supercell was constructed for doping using a single program calculation within the WIEN2k interface task module. The

selected RMT values for the Ba, Fe, O, and Sb atoms are 2.50, 1.90, 1.90, and 1.64, respectively. For Brillouin zone sampling, the Monkhorst–Pack scheme[52] was employed. A 10 × 10 × 10 *k*-point mesh was used for pure BFO, and a 7 × 7 × 7 *k*-point mesh was applied for both 12.5% and 25% doped configurations. For density of states (DOS) and optical property calculations, a denser mesh of 17 × 17 × 17 *k*-points was used to ensure higher accuracy. Optical properties were analysed by calculating the intraband contribution using the Drude model, where plasma frequency (ω_p) was extracted from the real part of the dielectric function.[53] The calculated plasma frequency for pure BFO is 3.372 eV, which shows a systematic decrease, with Sb doping 2.258 eV for 12.5% and 1.0548 eV for 25%. This behaviour is consistent with the well-known relationship between plasma frequency and electron density.[53] The calculation of thermoelectric transport properties was performed utilising the BoltzTraP2 code,[54] which deals with non-spin-polarized SCF calculations. A uniform *k*-point mesh of 12 × 12 × 12 was utilised for pure BFO, while a coarser grid of 7 × 7 × 7 was applied for the 12.5% and 25% Sb-doped supercells in the BoltzTraP transport calculations. Due to the cubic symmetry of the system, the physical properties along the *xx*-, *yy*-, and *zz*-axes were found to be equivalent. Hence, all results are presented in the *xx*-plane shown in the figure, encompassing the symmetry-equivalent crystallographic directions. Structural visualization and analysis were performed using the XCrySDen package.[55]

3. Results and discussion

3.1 Structural properties

The cubic structure of the lead-free Fe base perovskite BFO has the following structural parameters: $a = b = c = 3.97106$ Å and the space group $Pm\bar{3}m$ (no. 221).[56,57] The pure cell includes 5 atoms in a single formula unit, comprising one Ba, one Fe, three O atoms, and the Wyckoff locations (symmetry) Ba-1b ($m\bar{3}m$), Fe-1b ($m\bar{3}m$), and O-3d (4/*mmm*), which have fractional coordinates (0.5, 0.5, 0.5), (0, 0, 0) and (0.5, 0, 0), respectively. In order to dope the BFO perovskite, a supercell (2 × 2 × 2) that is 8.0 times larger than the primitive unit cell is constructed. Hence, the supercell of BFO consists of 40 atoms, comprising 8 Ba atoms, 8 Fe atoms and 24 O atoms. In the 12.5% doped structure, one Fe atom was substituted with one Sb atom, and in the 25% doped case, two Fe atoms were replaced by two Sb atoms. The current study demonstrates that the first-principles (*ab initio*) simulation is credible because the simulated findings remain approximately the same as the existing experimental results.[56] The calculated unit cell parameters of pristine and doped samples are represented in Table 1. It compares the lattice constants and unit cell volumes of pure supercell and Sb-doped perovskites. Table 1 shows that our predicted lattice parameters are consistent with prior experimental and theoretical results, demonstrating the accuracy of our computations (Fig. 1 and 2).[57,58]

Table 1 Optimized unit cell lattice parameters of pure and Sb-doped BFO perovskites

	Parameters		
Sample	a_o (Å)	V (Å^3)	Ref.
$BaFeO_3$	3.9585	62.0285	This work
	3.97106	62.6209	Expt.[56]
	3.95	61.6298	Th.[57]
$BaFe_{0.875}Sb_{0.125}O_3$	3.9973	63.8705	This work
$BaFe_{0.75}Sb_{0.25}O_3$	4.0326	65.5776	This work

It is important to understand that several factors influence the stability of perovskite oxides. One such element is the Goldschmidt tolerance factor (t)[59] and another one is octahedral factor $\sim\mu$.[60] The stability of the cubic structure has generally been examined by a qualitative examination of the $\sim t$ and $\sim\mu$ defined using the following equation:

$$t = \frac{(r_A + r_O)}{\sqrt{2}(r_B + r_O)}, \quad \text{(I)}$$

$$\mu = \frac{r_B}{r_O}, \quad \text{(II)}$$

where r_A, r_B and r_O are the radii of the A-site cation, B-site cation, and O^{2-} ion, respectively. Since the investigated material consists of more than three different atoms with mixed valence states of $Sb^{3+/5+}$ and $Fe^{3+/4+}$, the mixed valence ionic radius should be averaged (*i.e.*, $r_{Fe} = \frac{r_{Fe^{3+}} + r_{Fe^{4+}}}{2}$ and $r_{Sb} = \frac{r_{Sb^{3+}} + r_{Sb^{5+}}}{2}$). The percentage present of ionic radii r_{Fe} and r_{Sb} at the B-site should be multiplied by the averaged ionic radii to get the weighted average ($Fe_{w.avg}^{2+/3+}/Sb_{w.avg}^{3+/5+}$) and finally

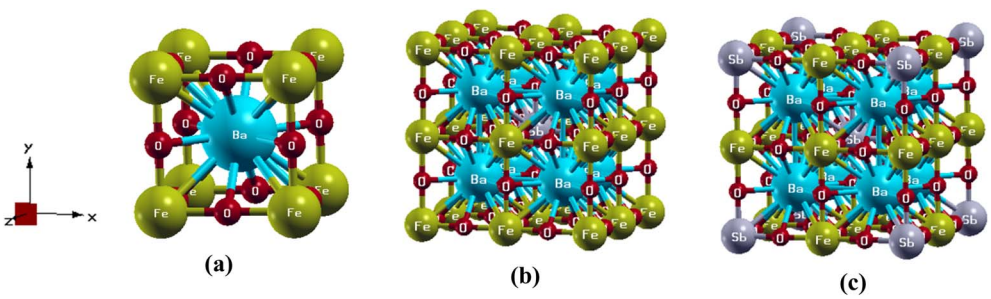

Fig. 1 Optimized cell structure of (a) pure BFO, (b) BFO with one Sb atom at the center of the supercell and (c) BFO with one Sb atom at the center and another one (one-eighth part) at the outer corners of the supercell.

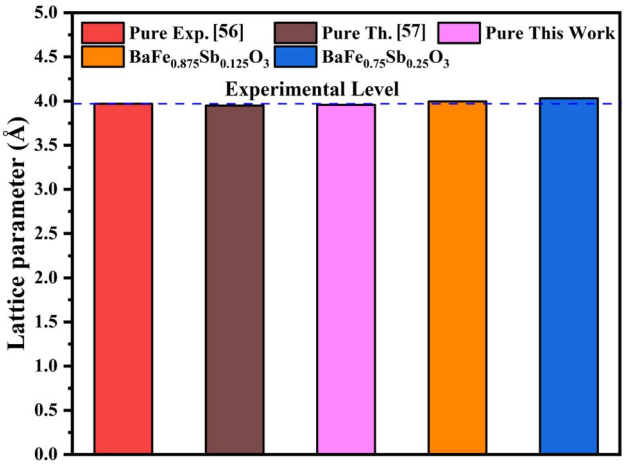

Fig. 2 Variation in lattice parameters among experimental, theoretical, and optimized BFO samples, as well as Sb-doped BFO sample.

sum the weighted average to obtain B-site radius r_B, (which is expressed as $r_B = (1 - x)r_{Fe} + xr_{Sb}$).

The material we investigate is cubic structured.[62,63] Hence, a cubic structure is expected to be stable in the range of $(0.77 < t < 1.05)$[59] and $(0.41 < \mu)$.[65] Based on Table 2, it is evident that pure and Sb-doped BFO are structurally stable. BFO is generally reported to crystallize in a hexagonal structure under ambient conditions. However, several studies have shown that a pseudo-cubic perovskite phase can be stabilized under conditions of high oxygen non-stoichiometry by employing specific oxidation pathways, such as the oxidation of $BaFeO_{2.5}$ into stoichiometric BFO.[66] In the present investigation, the structural stability of BFO and Sb-doped BFO was investigated by calculating the Goldschmidt tolerance factor values, as shown in Table 2. The tolerance factor values are within the range that is typically associated with perovskite stability, which implies that the cubic structure can be reasonably considered in the case of Sb doping. In the literature,[67] similar methods of tolerance factor analysis have been reported, in which phase stabilization was associated with structural distortions caused by oxygen stoichiometry and cation substitution. In contrast, the octahedral factor calculation is another verification of the cubic structure. Hence, octahedral factor coordination is feasible though a bit on the smaller side for a typical octahedral coordination factor. The structural stability and equilibrium volume of pure and Sb-doped BFO compounds were evaluated by fitting the total energy–volume data to the Murnaghan equation of state, as shown in Fig. 3(a–c). Fig. 3(a–c) presents the optimized curves for BFO and 12.5% and 25% Sb-doped BFO, respectively. In each instance, the total energy demonstrates a distinct minimum, signifying a clearly defined equilibrium state. The parabolic configuration of the curves indicates the mechanical stability of all three compositions. The equilibrium volume increases with higher Sb doping, which is consistent with the larger ionic radius of Sb^{5+} relative to Fe^{3+}. When Sb is added to the BFO, the volume grows and the total energy minimum becomes more negative. This means that the material is more thermodynamically stable.[68] The results confirm the thermodynamic feasibility of Sb substitution and demonstrate that all systems exhibit mechanical and energetic stability at optimized volumes. Detailed information is provided in the SI (Tables S1–S3).

3.2 Lattice distortion

One of the essential characteristics of a crystal is its lattice distortion. The lattice contraction or expansion caused by the doping element depends on its chemical connection with undoped elements, crystal structure, and relative atomic size.[61,69] Lattice distortion arises in $Ba_2Fe_{1-x}Sb_xO_3$ ($x = 0.125$ and 0.25) perovskites because of the outgoing atoms from the pure supercell caused by 12.5% and 25% Sb doping instead of Fe, respectively. The lattice distortion is therefore created because Sb and Fe have different atomic sizes. By comparing the parameters, we can determine the lattice distortion and compute the volumetric distortion. The more the lattice distortion, the less the conductivity.[70] Hence, we can calculate the volumetric distortion using the formula $\Delta = (V_{doped} - V_{pure})/V_{pure}$ and the linear distortion using the formula $\delta = (a_{doped} - a_{pure})/a_{pure}$. The volumetric and linear distortions of 12.5% and 25% Sb-doped BFO are presented in Table 3, where $\delta = \Delta/3$. Herein, Table 3 indicates the minimal lattice changes necessary

Table 2 Calculation of tolerance factor (t) and octahedral factor (μ) for pure and Sb-doped BFO

	Ionic radius, r (Å) (ref. 61)							
Sample	r_A	r_B		r_O	t	Ref.	μ	Ref.
$BaFeO_3$	Ba^{2+} 1.61	Fe^{3+} (HS) 0.645	Fe^{4+} (HS) 0.585	O^{2-} 1.40	1.056	This work	0.439	This work
		$Fe_{w.avg}^{2+/3+}$ (HS) (1×0.615)			1.066	Expt.[60,61]	$(0.41 < \mu)$	Th.[60,64]
$BaFe_{0.875}Sb_{0.125}O_3$	Ba^{2+} 1.61	Fe^{3+} (HS) 0.645 Fe^{4+} (HS) 0.585 $Fe_{w.avg}^{3+/4+}$ (HS) $(0.87 \times 0.615) = 0.538$	Sb^{3+} 0.76 Sb^{5+} 0.60 $Sb_{w.avg}^{3+/5+}$ $(0.125 \times 0.68) = 0.085$	O^{2-} 1.40	1.014	This work	0.445	This work
$BaFe_{0.75}Sb_{0.25}O_3$	Ba^{2+} 1.61	Fe^{3+} (HS) 0.645 Fe^{4+} (HS) 0.585 $Fe_{w.avg}^{3+/4+}$ (HS) $(0.75 \times 0.615) = 0.461$	Sb^{3+} 0.76 Sb^{5+} 0.60 $Sb_{w.avg}^{3+/5+}$ $(0.25 \times 0.68) = 0.17$	O^{2-} 1.40	1.048	This work	0.451	This work

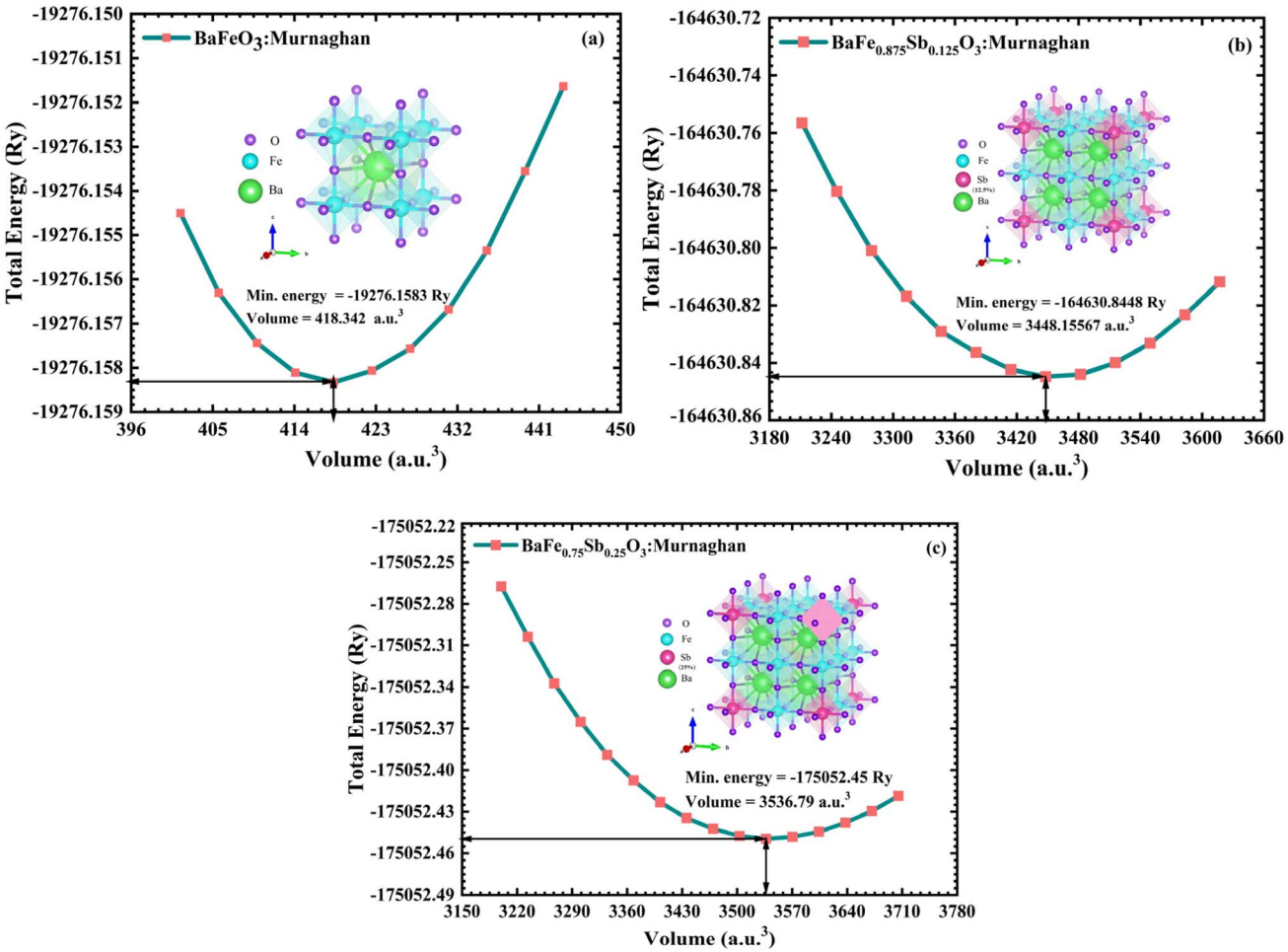

Fig. 3 Volume optimization of (a) pure and Sb-doped BFO samples with (b) 12.5% and (c) 25% doping concentrations.

for structural stability, where small δ and a minimal Δ value suggest that doping maintains the cubic phase and has little effect on the lattice, which is advantageous for stability. Therefore, linear distortion is far more significant than other types of distortion, while volumetric distortion is still marginally more essential. Lattice distortion increases the material's internal energy as well as its tiny stress. It resists dislocation and glide deformation, which boosts the material's strength and hardness.[71]

Table 3 shows that the computed lattice distortions exhibit a distinct rise with Sb doping. This clearly indicates that for the 12.5% Sb-doped BFO, the value of δ is 0.0098 and the value of Δ is 0.0297. The results increase to 0.0187 and 0.0572 for 25% Sb-doped BFO, signifying gradual lattice deformation resulting from the ionic radius discrepancy between Fe and Sb ions. Such distortions can modify the electrical bandwidth and coupling mechanisms, affecting both structural and thermoelectric properties. This corresponds with prior research indicating that doping-induced distortions significantly influence the physical behavior of perovskite systems.[72]

3.3 Electronic properties

This section presents a detailed analysis of the electronic band structures of BFO and its Sb-doped variants, with the aim of understanding their metallic behavior and changes in electronic transport properties. Fig. 4 illustrates the spin-polarized electronic band structures of BFO under three different doping conditions: no doping (Fig. 4a and b), 12.5% Sb doping (Fig. 4c and d), and 25% Sb doping (Fig. 4e and f). In all three cases,

Table 3 Calculation of lattice distortion for 12.5% and 25% Sb-doped BFO samples

Doping sample	Doping percentage	Linear distortion, δ	Volumetric distortion, Δ
$BaFe_{0.875}Sb_{0.125}O_3$	12.5%	0.0098	0.0297
$BaFe_{0.75}Sb_{0.25}O_3$	25%	0.0187	0.0572

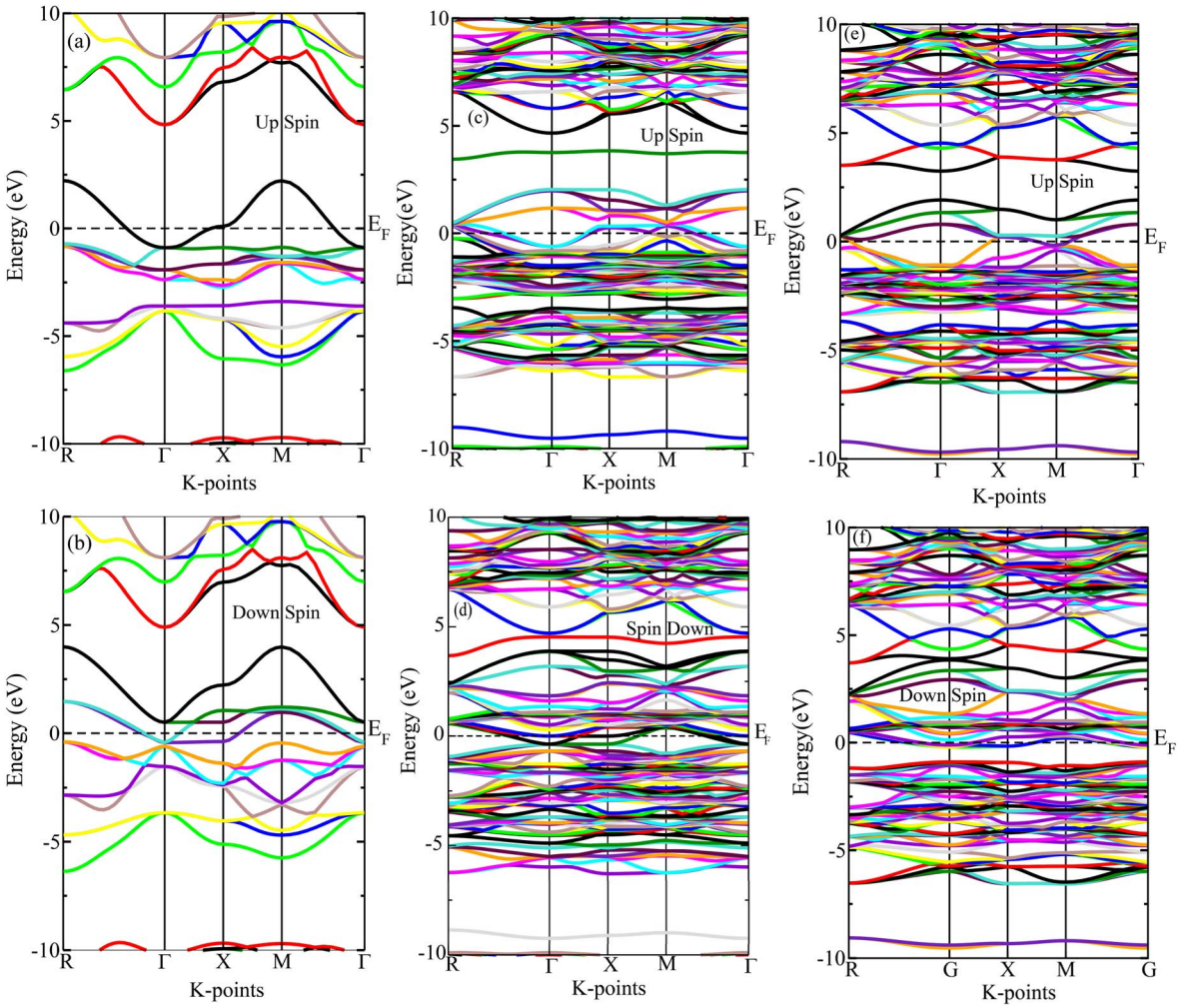

Fig. 4 Up spin and down spin band structures of BFO of three different types: (a and b) pure single cell, (c and d) 12.5% Sb-doped material and (e and f) 25% Sb-doped material.

both up-spin and down-spin channels exhibit distinct metallic characteristics, as evidenced by multiple bands crossing the E_F at the gamma point (Γ). The pure BFO system already demonstrates metallicity, which originates from the partially filled Fe 3d bands hybridized with O 2p orbitals, leading to significant electronic dispersion near E_F. This is consistent with prior theoretical and experimental findings reporting metallic or weakly correlated metallic behavior in cubic and tetragonal BFO phases.[73,74] Upon substituting Fe with Sb at a concentration of 12.5%, the electronic band structure becomes increasingly complex. The E_F remains crossed by multiple spin-polarized bands in both channels, confirming the preservation of metallicity. The emergence of additional dispersive states around E_F indicates enhanced electronic hybridization and charge carrier redistribution introduced by Sb 5s and 5p states. The increased density of states (DOS) at the E_F suggests a potential improvement in electrical conductivity and modified magnetic interactions, which are sensitive to the local electronic environment around the Fe and Sb atoms.[75] Further increasing the Sb doping concentration to 25% results in even denser band populations near E_F for both spin channels. The overlapping electronic states reinforce the metallic nature and point toward a more delocalized conduction mechanism. This enhancement in metallic behavior is likely due to the electron-donating role of Sb, which contributes to filling Fe-derived conduction bands and alters Fe–O–Sb bonding pathways. This kind of tuning ability of the electronic structure through substitutional doping is a good way to make perovskite-based oxides that can perform more advanced electronic, magnetic, or catalytic tasks.[76] This is also confirmed by the density of states (DOS) calculation illustrated in Fig. 5. The calculation of DOS shows how the band structure (valence band and conduction band) and electron-occupied orbitals are related. Fig. 5 depicts both the spin-up and spin-down DOS representations. As depicted in Fig. 5, the BFO cell exhibits ferroelectric characteristics that are vital for spintronic and multiferroic devices.[77] Fig. 5(a–d) shows the total and partial density of states (DOS) for pure BFO and its 12.5% and 25% Sb-doped BFO. The vertical dashed red line corresponds to the Fermi level (E_F), which has been set to zero energy for reference. The DOS for pure BFO (Fig. 5(a)) shows a limited

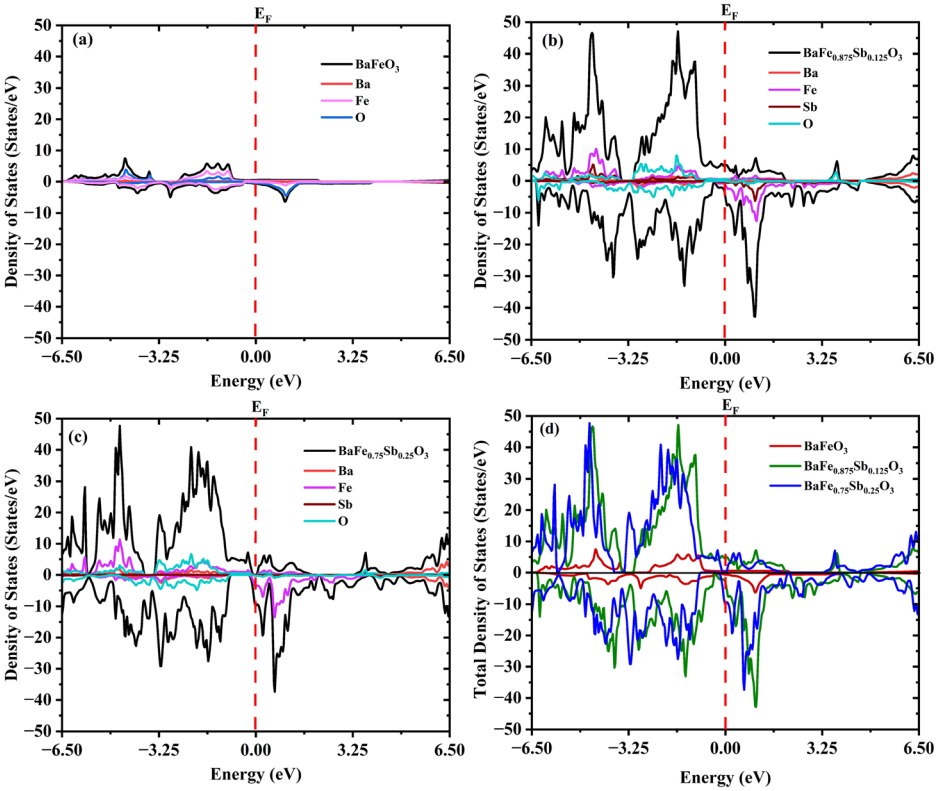

Fig. 5 PDOS and TDOS of BFO determined through simulation utilizing (a) pure single cell, (b) 12.5% Sb-doped sample, (c) 25% Sb-doped sample and (d) comparison of total DOS for pure and Sb-doped BFO samples.

density at the E_F, which confirms that it is a metal. The Fe-3d states hybridised with O-2p orbitals around E_F gives it metallic character. As expected, the contributions from Ba atoms are quite small since they have a closed-shell electronic structure. When Sb is added, the DOS profiles vary a lot, as shown in Fig. 5(b–d). The DOS at E_F notably increases for 12.5% Sb doping due to large contributions from the Fe-3d and Sb-5p states. This shows that the electronic delocalisation has increased and the carrier density has grown, which is consistent with the increases in electrical conductivity and power factor observed in the thermoelectric analysis. The trend continues with more doping, with 25%, where the total DOS at E_F continues to increase and the Fe and Sb states remain the predominant contributors around the Fermi level. This result is also shown in Fig. 6. The progressive rise in DOS at E_F supports the enhanced thermoelectric performance that comes from having more carriers, which is directly related to higher Seebeck coefficients and power factors. Additionally, the Sb substitution seems to impact the electronic environment around the Fe atoms, which could affect exchange contacts and magnetic ordering because the Fe-3d and Sb-5p orbitals overlap. These exchange contacts and magnetic ordering are shown in Fig. 8. However, doping the B site to change the electrical characteristics is a common way to change the functional properties of perovskite oxides.[78]

Sb contributes to filling Fe-derived conduction bands and alters Fe–O–Sb bonding. The projected density of states (PDOS) analysis shown in Fig. 6 clearly demonstrates orbital hybridizations in both pure and Sb-doped BFO. Each subfigure illustrates the contributions of distinct elements and multi orbital hybridization among them.[79] In the pure BFO system (Fig. 6(a–c)), the Ba-6s state contribution in Fig. 6(a) shows a negligible contribution, with activity mainly deep in the valence band, indicating their limited role in electronic transport. The Fe-3d states in Fig. 6(b) strongly hybridize with the O-2p orbitals shown in Fig. 6(c) near the E_F. Among them, the Fe-3d_{eg} orbitals (d_{z^2} and $d_{x^2-y^2}$) exhibit direct overlap with the O-2p orbitals along the Fe–O bond axis corresponding to σ-type bonding interactions. In contrast, the Fe-3$d_{t_{2g}}$ orbitals (d_{xy}, d_{yz}, and d_{zx}) overlap laterally with the O-2p orbitals corresponding to π-type bonding. This σ–π hybridization is a key feature in transition metal oxides, where σ bonds dominate structural stability and π bonds play an important role in conduction and magnetic exchange.[80] This hybridization mediated by Fe–O–Fe superexchange interactions is a key driver of the material's electronic conductivity in its cubic perovskite phase.[81] For the 12.5% Sb-doped BFO system (Fig. 6(d–g)), the Ba-6s contribution in Fig. 6(d) remains minor and does not participate actively in the conduction band. The Fe-3d orbitals remain significant in the conduction bands, especially the Fe-3$d_{t_{2g}}$ orbitals. The O-2p states continue to show interaction with Fe-3d states, and the overlap remains important for σ-type bonding. However, the O-2p contribution becomes more spread out with doping, showing increased mixing with Sb-5d orbitals. The Sb-4d

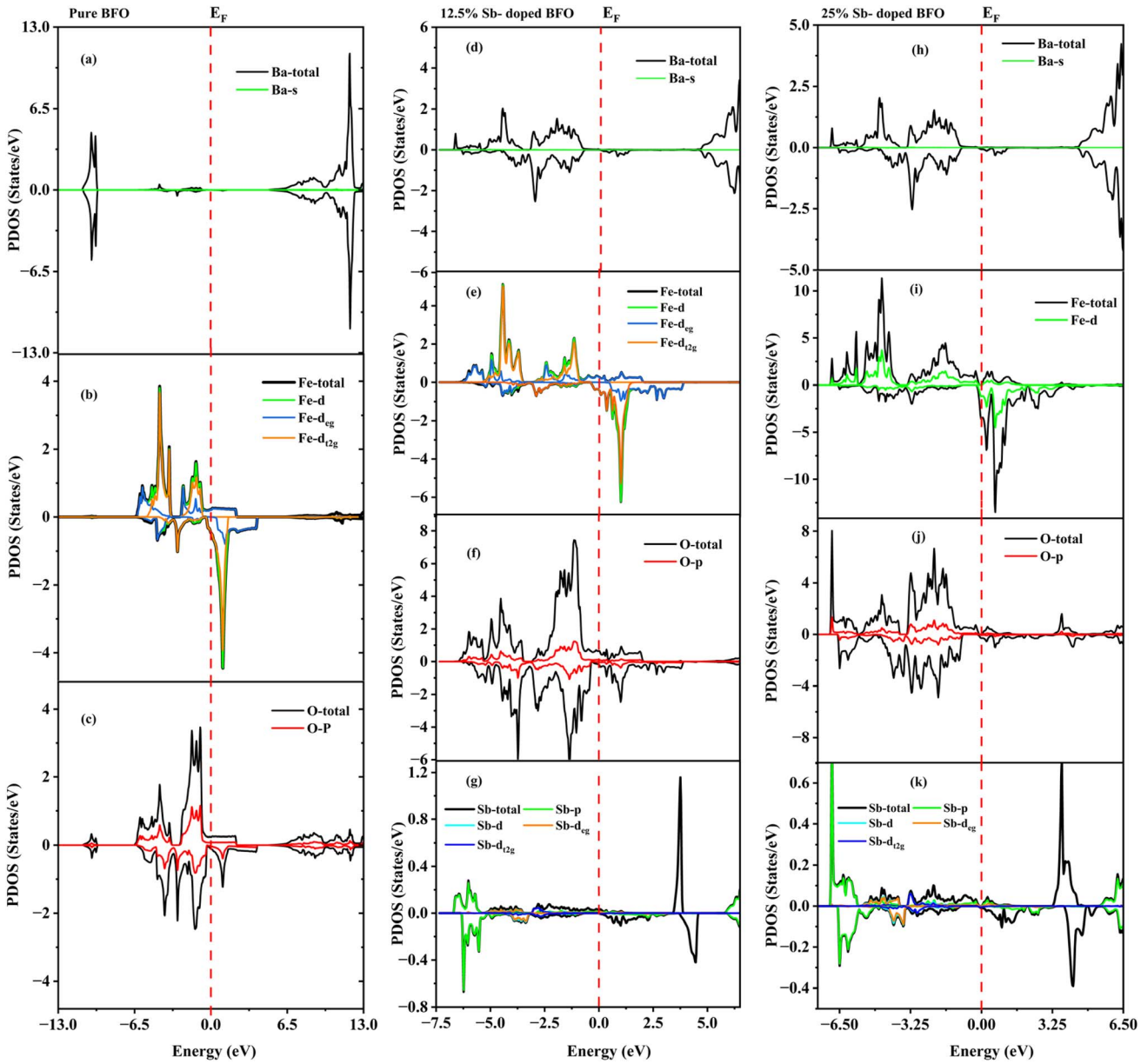

Fig. 6 PDOS of BFO: (a–c) pure single cell, (d–g) 12.5% Sb-doped sample and (h–k) 25% Sb-doped sample.

orbitals from Fig. 6(f) overlap significantly with the O-2p states shown in Fig. 6(g), especially near E_F. Moreover, the Sb-5s and Sb-5p states contribute at deeper energies, reinforcing Fe–O–Sb covalency. The σ-type Fe-3d and O-2p overlap remains evident, but additional hybridization with the Sb states modifies the conduction pathways. Importantly, the Sb-5p and Sb-5d orbitals illustrated in Fig. 6(g) introduce states close to the conduction band minimum, suggesting potential alterations in carrier concentration and mobility. Such doping-induced modifications have been shown to tune thermoelectric and magnetic properties in perovskite oxides.[82] For the 25% Sb-doped BFO system illustrated in Fig. 6(h–k), the Ba-6s contribution in Fig. 6(h) shows a very weak contribution again, without much shift compared to the pure BFO system. It remains a spectator in the conduction properties. From Fig. 6(j and k), the PDOS shows stronger Sb–O hybridization and a redistribution of Fe-3d states near E_F. This redistribution reduces the dominance of the Fe-3d states illustrated in Fig. 6(i) in the PDOS study at E_F. This aligns with the observed trends of lowering plasma frequency and weakening metallicity. In this case, σ-type interactions (Fe-3d_{eg}–O-2p and Sb–O) continue to stabilize the lattice, while π-type Fe-3$d_{t_{2g}}$–O-2p contributions remain essential for electronic conduction. These features suggest that higher Sb doping could induce carrier localization, thereby affecting both the transport and magnetic characteristics of the system, as similarly observed in other Sb-doping perovskites.[83] Overall, the DOS-PDOS analysis reveals that Fe-3d and O-2p hybridization is the primary contributor to the electronic states near E_F in pure BFO. Sb doping modifies this interaction in a concentration-dependent manner; moderate doping (12.5% Sb-doped BFO)

shifts the spectral features while preserving hybridization, while higher doping (25% Sb-doped BFO) introduces stronger Sb-derived states and decreases the Fe–O contributions, offering significant implications for tuning the material's thermoelectric and magnetic performance.[84]

3.4 Optical properties

Characterization of optical properties is integral for optimizing the performance and functionality of optoelectronic devices. To describe how a material interacts with electromagnetic radiation, optical parameters such as absorption, optical conductivity, reflectivity, dielectric function, refractive index and energy loss function are explained in this section. Fig. 7(a and b) present the optical conductivity of the BFO and its Sb-doped variants as a function of photon energy (eV) and wavelength (nm). Optical conductivity reflects how well a material conducts electric current under an oscillating electromagnetic field and is directly linked to the density of states, which allows optical transitions. In the infrared region, corresponding to photon energies below 1.77 eV, the optical conductivity is minimal for all compositions. This indicates that intraband (Drude) contributions are suppressed due to strong carrier scattering or low free-carrier coherence.[85] As photon energy enters the visible spectrum, a noticeable rise in optical conductivity is observed, especially for pure BFO. This increase results from direct interband transitions between occupied and unoccupied states near the Fermi level. Interband and intraband transitions dominate the optical behavior of a metallic solid in the higher and lower energy regions, respectively.[86] The magnitude of conductivity here suggests strong light-matter interaction, making the material suitable for optoelectronic applications, such as UV photodetectors, sensors and solar cells.[87] The introduction of Sb at the Fe sites leads to a reduction in overall optical conductivity, which becomes more pronounced with increased Sb content. Sb^{5+} ions contribute additional electrons and alter the local electronic structure. These electrons may partially fill available states, reduce the number of transitions and increase carrier scattering. As a result, the material becomes less optically conductive in the visible range. In the UV region at 4–9 eV, multiple conductivity peaks appear. Pure BFO generally maintains higher conductivity than its doped variants, which is consistent with its delocalized electronic structure and

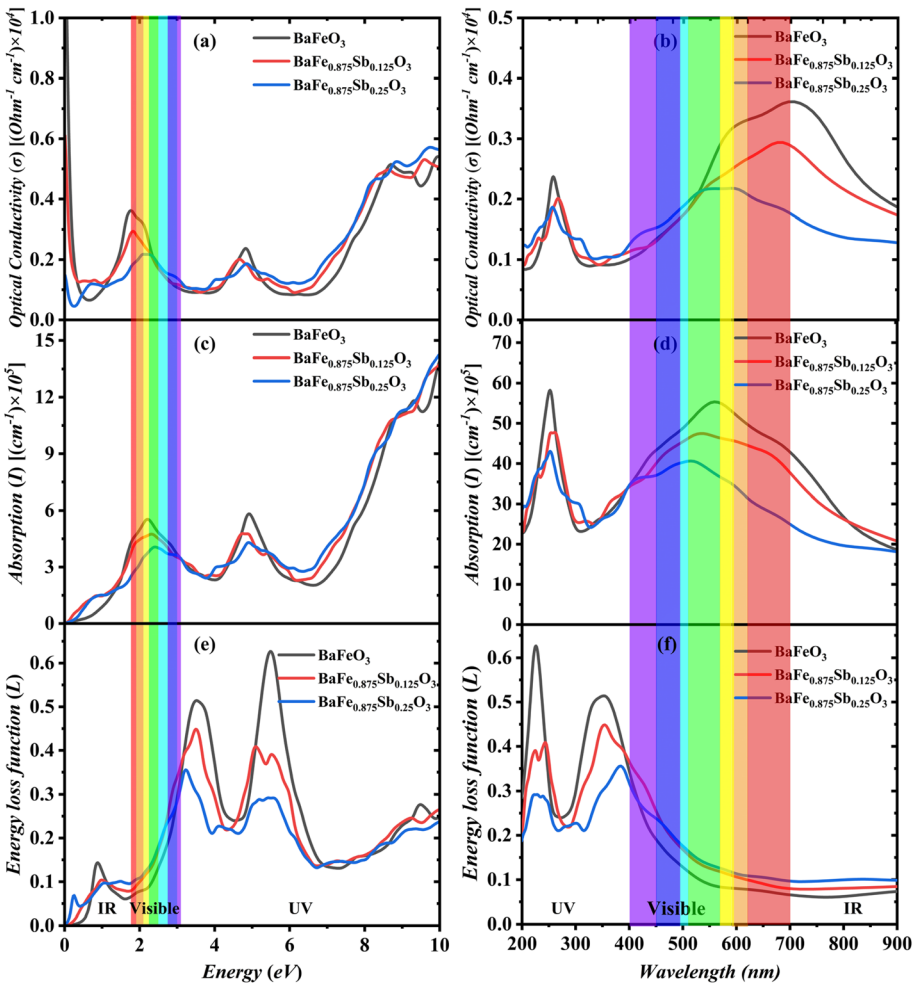

Fig. 7 Simulated energy and wavelength diagram for (a and b) optical conductivity, (c and d) absorption, and (e and f) energy loss functions of pure BFO and Sb-doped BFO samples.

greater transition probability. However, at around 10 eV, the trend reverses. Both Sb-doped samples, especially 25% doped BFO, exhibit higher optical conductivity than pure BFO. The wavelength-based plot in Fig. 7(b) reinforces these observations by mapping the energy values to the electromagnetic spectrum. The optical conductivity is highest in the UV and visible ranges for BFO, but as one moves to shorter wavelengths, the Sb-doped samples begin to exhibit stronger responses. Fig. 7(c) and 6(d) show the absorption coefficient, which is crucial for optoelectronic devices, specifically for solar cells, because it shows how efficiently a material can absorb light.[88] In the IR region, the absorption coefficient remains low, as metals typically reflect most incident light and do not support significant interband transitions at low photon energies. In other words, a lower absorption coefficient corresponds to higher transparency, as the photons do not possess sufficient energy to induce significant electronic transitions. As energy increases in the visible and UV ranges, absorption rises due to enhanced interband transitions. The pure sample shows the earliest and most significant increase, while Sb doping shifts absorption to higher energies and reduces its intensity. This suggests that doping alters the density of states near the E_F and reduces the probability of interband transitions. In the UV region, all samples are absorbed strongly, but pure BFO still shows the highest intensity, indicating better performance in UV light applications. The wavelength-based plot clearly shows this inverse relationship; as wavelength decreases, absorption increases, particularly in the UV region. This also visually emphasizes the blue shift caused by doping, as the doped curves shift left compared to the pure one. Additionally, from Fig. 7, it is evident that the trends in photoconductivity and absorption are closely aligned, indicating that enhanced absorption contributes directly to increased photoconductivity.[89] Fig. 7(e) and 6(f) show the energy loss function (L) as a function of photon energy and wavelength. The loss function is an important parameter that describes the energy dissipation of a fast electron travelling through the material.[90] The peaks in this function are related to plasma resonances, and the corresponding frequency is referred to as the plasma frequency.[91] In the IR and visible regions, the loss function remains low for all compositions, indicating weak plasmonic activity and minimal dielectric losses, likely due to low free carrier density. However, in the UV region, a distinct

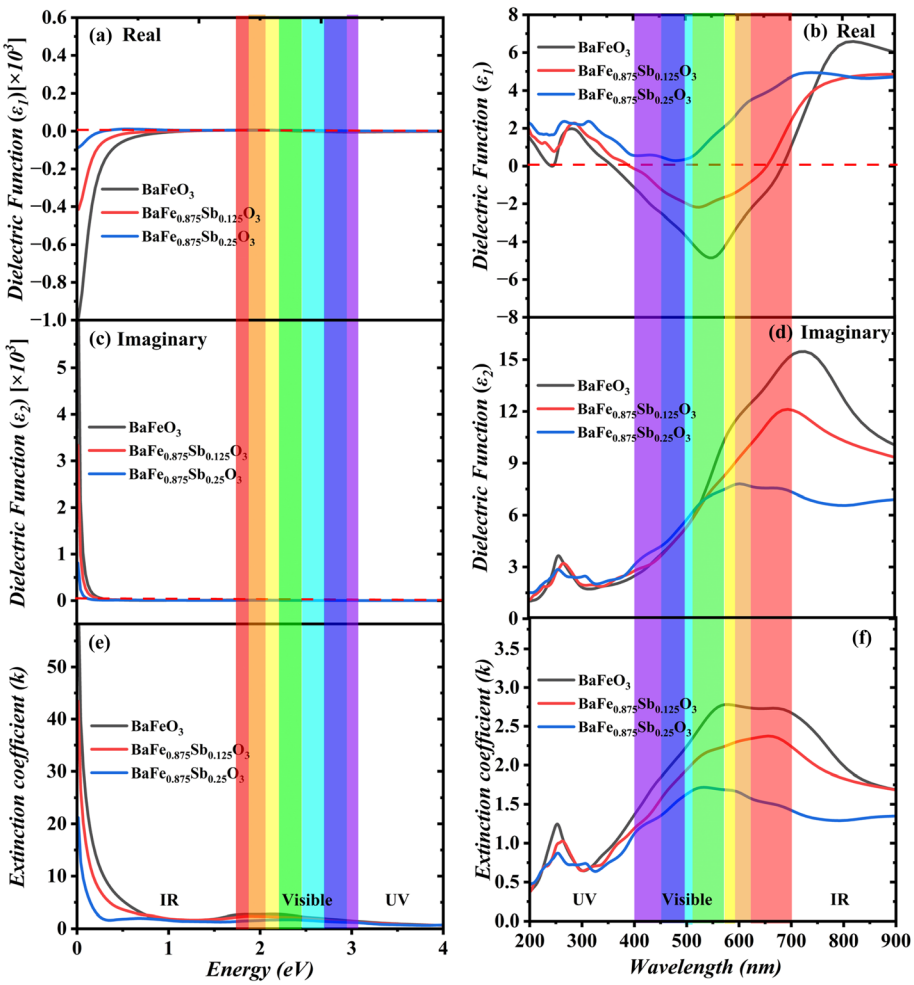

Fig. 8 Simulated energy and wavelength diagram for (a and b) dielectric function real part, (c and d) dielectric function imaginary part, and (e and f) extinction coefficient of pure BFO and Sb-doped BFO samples.

peak emerges around 6–8 eV, representing the bulk plasma frequency, the energy where collective oscillations of electrons are most pronounced. Among all, BFO exhibits the most prominent peak, suggesting stronger plasmonic behavior. In contrast, the observed decrease in the plasmon peak when Sb is added aligns with accepted models of carrier-induced optical damping in disordered materials.[92]

Fig. 8(a–f) illustrates both the real and imaginary parts of the dielectric function $\varepsilon(\omega)$ and the extinction coefficient (k) for both pure and Sb-doped BFO, which are analysed across the energy and wavelength domains. The real component of the dielectric function, $\varepsilon_1(\omega)$ illustrated in Fig. 8(a) and (b), describes the material's polarisation response to an external electromagnetic field. In the low-energy infrared region, pure $BaFeO_3$ demonstrates a markedly elevated $\varepsilon_1(\omega)$, which experiences an abrupt decrease as it approaches the visible and ultraviolet regions. The introduction of Sb doping significantly suppresses this peak, resulting in a nearly flat real part across the spectrum, particularly observed in 25% Sb-doped BFO. This reduction indicates diminished dielectric screening, decreased polarisability, and a lower concentration of free carriers resulting from the structural and electronic changes caused by Sb doping.

The imaginary component $\varepsilon_2(\omega)$, illustrated in Fig. 8(c) and (d), reflects the absorption characteristics associated with interband transitions. Pure BFO exhibits a significant peak in the ultraviolet region, indicating robust optical absorption. With an increase in Sb content, there is a decrease in both the intensity and breadth of the absorption feature, indicating a reduction in oscillator strength and a limited number of allowed transitions at elevated energy levels. This observation aligns with the noted reduction in the density of states at the conduction band edge and corresponds with the trends of a lower extinction coefficient. Fig. 8(e) and (f) illustrate the extinction coefficient $k(\omega)$, which is directly associated with the optical absorption of the material. In the energy-dependent plot, pure BFO demonstrates a pronounced extinction response in the infrared region, subsequently exhibiting a sharp decrease across the visible and ultraviolet ranges. Sb doping markedly reduces the magnitude of k across all wavelengths. 25% Sb-doped BFO exhibits a more gradual and flatter extinction curve, indicating enhanced optical transparency and reduced free carrier absorption. This is further reinforced by a corresponding decrease in reflectance and refractive index, confirming the argument that Sb-induced disorder effectively attenuates electronic oscillations. The optical constants obtained from $\varepsilon_1(\omega)$, $\varepsilon_2(\omega)$ and $k(\omega)$ demonstrate that Sb doping reduces the dielectric and absorption characteristics of pure BFO, thereby improving its transparency and tunability for use in transparent conducting oxides and photonic filters.[93] The findings align with classical electrodynamics, indicating that doping-induced carrier depletion and enhanced scattering attenuate plasmonic and absorption-related characteristics.[94] Fig. 9(a)–(d) illustrates the optical behavior of pure and Sb-doped BFO in the reflectivity and refractive index spectra across the energy and wavelength regions. Fig. 9(a) presents the reflectivity spectra, demonstrating that pure BFO samples show a pronounced peak in the infrared (IR) region, achieving a maximum reflectivity close to 0.9, which is subsequently followed by a steep decline in the visible and ultraviolet (UV) regions. Following the introduction of Sb doping, there is a notable decrease in reflectivity throughout the entire spectrum. The suppression increased with increased Sb concentration, especially at 25% Sb doping, suggesting a decrease in free

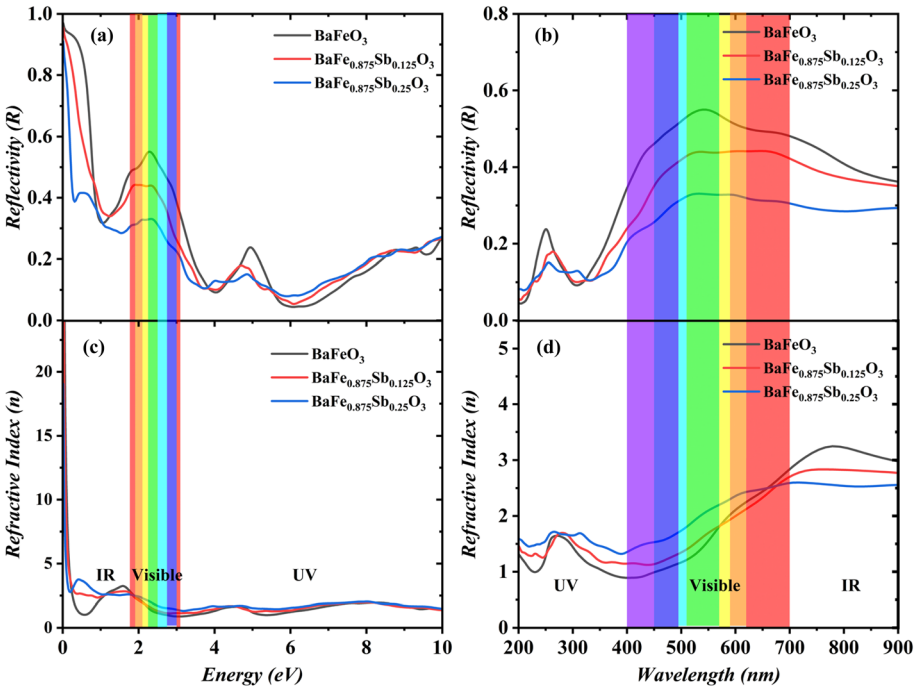

Fig. 9 Simulated energy and wavelength diagram for (a and b) reflectivity, and (c and d) refractive index of pure BFO and Sb-doped BFO samples.

carrier density and a dampening of collective electronic oscillations. Similar trends are noted in the wavelength-dependent reflectivity, as shown in Fig. 9(b), where the doped samples exhibit lower reflectivity throughout the visible and near-IR regions, indicating improved optical transparency. The refractive index (n), illustrated in Fig. 9(c and d), experiences notable changes due to doping. The energy-dependent plot presented in Fig. 9(c) shows that pure BFO exhibits a distinct peak in the IR region, where n is greater than 20, indicating pronounced dispersion and optical confinement. The peak is significantly diminished in the doped systems, as evidenced by n falling below 10 for 25% Sb-doped BFO, which aligns with a decrease in polarizability and carrier concentration. The refractive index across the visible and UV regions exhibits a relatively consistent profile for all compositions although the doped samples present marginally lower values, confirming the noted decrease in reflectivity. The observed trends indicate that the substitution of Sb leads to a weakening of the dielectric response. This occurs through modifications in charge density distribution and an increase in electronic scattering, both of which work together to suppress plasmonic features and diminish the strength of light–matter interactions. The adjustment of optical constants is essential for the advancement of transparent conducting oxides and infrared-filter materials.[94]

3.5 Electron charge density analysis

Fig. 10 shows the electron density plots of the pure BFO and its Sb-doped counterparts. Fig. 10(a) shows the electron density of pure BFO, while the electron distribution around the Ba, Fe and O atoms is clearly visible. The highest electron density is observed around the Ba atom, with surrounding electron density peaks around the Fe and O atoms. The Ba^{2+} ion donates electrons to the oxygen atom, leading to a largely ionic bond between Ba and O. The Ba–O bond is predominantly ionic. Moreover, the Fe–O bond shows some degree of covalency due to the d-orbitals of Fe participating in bonding with the p-orbitals of O. Hence, the Fe–O bond exhibits a mixed ionic-covalent character. Fig. 10(b) shows the electron density of 12.5% Sb-doped BFO, while the increased electron density around the Sb site indicates charge redistribution due to doping, with noticeable changes in the local charge environment of the Fe and O atoms. The Fe–Sb bond likely exhibits a covalent character due to the overlap of the Fe-3d orbital and Sb-5p orbital. The high electronegativity of Sb could draw some charge towards itself, which in turn could induce a slight redistribution of charge around Ba and its nearby O atoms. The Sb ionic size and charge may also influence the local coordination environment, potentially weakening some Fe–O bonds and altering the Ba–O interactions. Fig. 10(c) shows the electron density of the 25% Sb-doped BFO, which reveals significant electron density redistribution due to the Sb-doping. The Sb atoms, being more electronegative than Fe, attract electron density, leading to a reduction in electron density around Fe and a more ionic Fe–O bond. Additionally, Sb–O bonds are more covalent with electron density transferred to the Sb site, enhancing the covalent nature of the Sb–O interaction. This redistribution is more pronounced compared to the 1 Sb-doped system (12.5% Sb-doped), showing stronger effects on local bonding and charge environments.

3.6 Magnetic properties

Fig. 11 shows the spin magnetic moment of the pure and Sb-doped BFO samples. Pure BFO shows a total magnetic moment of 3.69μ_B per formula unit observed in the unit cell, which is consistent with prior reports of ferromagnetic ordering primarily localized at Fe sites due to mixed valence Fe^{3+}/Fe^{4+} states.[95] By constructing a 2 × 2 × 2 supercell (40 atoms, 8 Fe sites) and doping 1 Fe with Sb (12.5% doping), the total magnetic moment increases to 27.73μ_B, with a noticeable

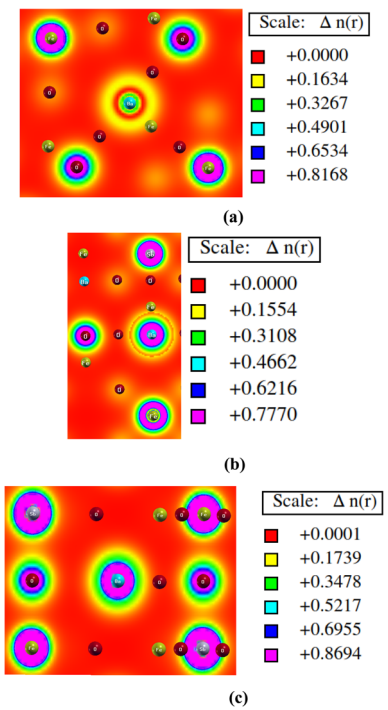

Fig. 10 Electron charge density distribution of BFO for (a) pure, (b) one Sb-doped (12.5%) and (c) two Sb-doped (25%) systems.

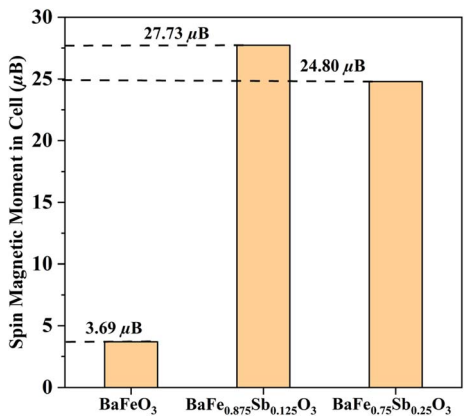

Fig. 11 Calculated spin magnetic moment for pure, 12.5% Sb-doped BFO and 25% Sb-doped BFO samples.

contribution from the interstitial region (1.60576μ_B). However, with 2 Sb atoms (25% doping), the total magnetic moment decreases to 24.80μ_B with a reduced contribution from the interstitial region (1.60576μ_B), indicating that excessive Sb substitution begins to disrupt Fe–O–Fe magnetic exchange pathways. The majority of the magnetic moment in pure BFO is carried by the Fe atoms although covalent Fe–O interactions cause the O atoms to show tiny induced moments. The magnetic moments of Fe atoms marginally decrease with Sb doping, indicating a weakening of the Fe–O exchange interactions. In the unit cell of the pure BFO system, the spin magnetic moment is 3.69μ_B, with a distribution of moments across various Fe atoms. When Sb is introduced at the 12.5% doping level, the magnetic moment of Fe in the region surrounding the Fe atom (referred to as sphere 3 in the calculation) decreases slightly to 3.34μ_B. At the 25% doping level, the Fe magnetic moments further decrease with values such as 3.28μ_B in sphere 3. Here, the term 'sphere' refers to a defined region around each Fe atom, within which the magnetic moment is calculated. This reduction in Fe magnetic moments could reflect a modification of the Fe 3d electronic structure due to the influence of Sb. There is a slight increase in the magnetic moments of O when Sb is doped. The O magnetic moment in the pure BFO system is 0.166μ_B, which is the usual value for Fe–O interaction.[96] In a 12.5% doping system, the magnetic moment of O in the region surrounding the O atom (referred to as sphere 7 in the calculation), the O magnetic moment marginally increases to 0.184μ_B. The oxygen magnetic moment reaches 0.187μ_B in sphere 7 when the Sb doping concentration is 25%. Here, the term 'sphere' refers to a defined region around each O atom,

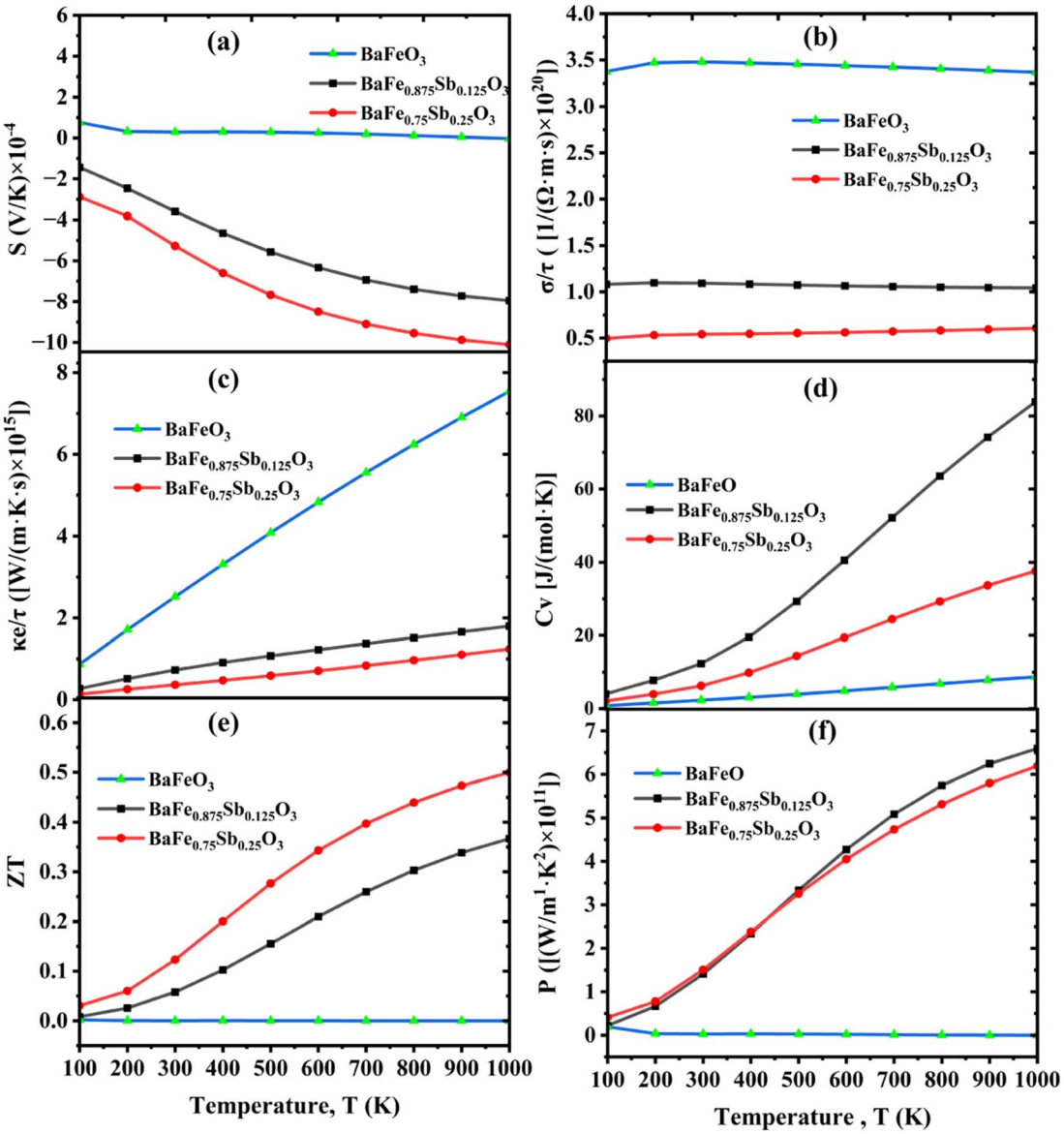

Fig. 12 Computed (a) Seebeck coefficient (S), (b) electrical conductivity (σ/τ), (c) thermal conductivity (κ_e/τ), (d) specific heat capacity (C_v), (e) figure of merit (ZT) and (f) power factor (P) for pure, 12.5% Sb-doped and 25% Sb-doped BFO samples.

within which the magnetic moment is calculated. The covalent bond between Fe and O atoms significantly influences the magnetic properties of BFO. In the pure system, there is a strong interaction between the Fe 3d and O 2p orbitals, resulting in notable magnetic coupling. When Sb substitutes for Fe, the characteristics of the Fe–O bonding are altered due to the differing electron configuration of Sb. The 5s and 5p orbitals of Sb exhibit greater localization and weaker hybridization with the 2p orbitals of O compared to the 3d orbitals of Fe. The reduction in Fe–O covalent interaction diminishes the bonding strength between Fe and O as the Sb concentration increases. This process aligns with previous DFT studies where the replacement of magnetic cations by non-magnetic species in perovskite ferrites led to a suppression of net magnetic moments due to the dilution of exchange interactions.[97] The decrease in the magnetic moment after doping with Sb atoms suggests that the electronic interactions may have weakened, potentially altering the material's magnetic properties.[98] This weakening of interactions could reduce the alignment or strength of the magnetic moments, ultimately affecting the overall magnetization of the Sb-doped BFO. Hence, the non-magnetic Sb doping levels can make the magnetic coupling in the lattice less stable.

3.7 Thermo-electrical properties

The thermoelectric performance of BFO, 12.5% and 25% Sb-doped BFO, is investigated using semi-classical Boltzmann transport theory under the constant relaxation time approximation (RTA), as implemented in the BoltzTraP2 code.[99] The figure of merit ZT, which defines thermoelectric efficiency, is given by

$$ZT = (S^2\sigma T)/\kappa$$

where S is the Seebeck coefficient, σ is the electrical conductivity, T is the absolute temperature, and κ is the total thermal conductivity. Fig. 12(a) illustrates that the Seebeck coefficient S in pure BFO remains low and positive, indicating weak p-type behavior. With Sb doping, S becomes negative and increases in magnitude, reaching -9.88 μV K^{-1} for 25% Sb-doped BFO at 900 K. This polarity reversal indicates a shift to n-type conduction, indicating that electrons are the dominant carriers. The increase in $|S|$ is attributed to modifications in the band structure near the Fermi level and enhanced carrier energy filtering due to Sb-induced potential fluctuations.[100] The electrical conductivity scaled by relaxation time (σ/τ), as illustrated in Fig. 12(b), decreases from 3.479×10^{20} Ω^{-1} m^{-1} s^{-1} in pure BFO to 5.41×10^{19} Ω^{-1} m^{-1} s^{-1} in 25% Sb-doped BFO. This decline is attributed to impurity scattering from Sb doping, which lowers carrier mobility. Correspondingly, the electronic thermal conductivity κ_e/τ, as depicted in Fig. 12(c), also decreases, which is consistent with the Wiedemann–Franz law.[100]

The specific heat capacity (C_v), as illustrated in Fig. 12(d), increases slightly with doping, which is consistent with enhanced carrier–lattice interactions. However, Fig. 12(f) illustrates a significant rise in power factor ($S^2\sigma/\tau$), reaching 6.24×10^{11} W m^{-1} K^{-2} for 25% Sb-doped BFO compared to 6.81×10^{7} W m^{-1} K^{-2} for pure BFO at 900 K. This enhancement arises from the increased $|S|$ illustrated in Fig. 12(a) despite a moderate drop in σ/τ according to Fig. 12(b). Additionally, there is a comparable ascending trend of the power factor, as illustrated in Fig. 12(f), corresponding to the temperature range from 200 K ($P = 0.774 \times 10^{11}$ W m^{-1} K^{-2}) to 500 K ($P = 3.254 \times 10^{11}$ W m^{-1} K^{-2}). In practical thermoelectric applications, a ZT value of approximately 1 is regarded as optimal.[100] Hence, ZT, as shown in Fig. 12(e), improves sharply, reaching 0.5 for 25% Sb-doped BFO at 900 K. This value is over 56 000 times greater than that of pure BFO, which has a ZT of approximately 8.88×10^{-6}. This places Sb-doped BFO within the range of promising candidates for medium-temperature thermoelectric energy conversion, particularly in waste heat recovery modules operating near 800–900 K.[101]

4. Conclusion

In this study, the electronic structure, mechanical stability, optical, magnetic and thermoelectric properties of non-toxic pure BFO and its Sb-doped (12.5% and 25%) were systematically investigated using first-principles calculations. The FP-LAPW method, implemented in the WIEN2k code, was employed within the framework of the DFT. The structural stability of all the compounds was verified through the Goldschmidt tolerance factor (τ) and octahedral factor (μ), which yielded values of 1.056 and 0.439 for pure BFO, 1.014 and 0.445 for 12.5% Sb-doped BFO, and 1.048 and 0.451 for 25% Sb-doped BFO, respectively. All three compositions were found to crystallize in the cubic $Pm\bar{3}m$ space group (no. 221). This study significantly advances our understanding of the effect of doping on material structure and its role in modifying the optoelectronic properties of iron oxide perovskites. According to the results of the electronic band structure calculations, all three compounds behave metallically before and after doping. Optical investigation demonstrated significant absorption in the UV spectrum, validating the suitability of these materials for optoelectronic applications. All compositions demonstrate metallic behavior, with an enhanced density of states at the Fermi level due to Sb doping, which contributes to improved thermoelectric properties. Sb doping results in a significant decrease in plasma frequency, dielectric constant, extinction coefficient, and absorption strength, suggesting a reduction in free carrier density and an improvement in optical transparency. The thermoelectric figure of merit (ZT) increases from nearly zero in pure BFO to about 0.37 and 0.50 for 12.5% and 25% Sb-doped BFO, respectively. These findings signify a substantial improvement in thermoelectric efficiency by tuning BFO with B-site Sb doping, especially for high-temperature waste heat recovery systems, transparent conducting oxides (TCOs), and IR filter coatings.[102] 25% Sb-doped BFO shows a reduction in the optical absorption and offers high optical transparency in the visible region, as evidenced by a reduced plasma frequency (less than the visible range energy). These properties are typical of materials that can function as TCOs, where the balance between conductivity and optical transparency is crucial. Thus, 25% Sb-doped BFO could still be

considered for TCO applications. In conclusion, this study establishes Sb-doped BFO as a versatile perovskite oxide with promising applications in energy and optoelectronic technologies.

Conflicts of interest

The authors declare no conflict of interest.

Data availability

Data will be made available on request.

Supplementary information: (i) S1.1 volume optimization methods, (ii) S1.2 optical constants calculation methods, (iii) S1.3 magnetic moments calculation method, and (iv) S1.4 thermoelectric properties calculation methods; also complete energy–volume data tables for undoped and Sb-doped $BaFeO_3$. See DOI: **https://doi.org/10.1039/d5ra06101f**.

References

1 M. A. Peña and J. L. G. Fierro, Chemical Structures and Performance of Perovskite Oxides, *Chem. Rev.*, 2001, **101**, 1981.
2 T. Kida, D. Takauchi, K. Watanabe, M. Yuasa, K. Shimanoe, Y. Teraoka and N. Yamazoe, Oxygen Permeation Properties of Partially A-Site Substituted $BaFeO_{3-\delta}$ Perovskites, *J. Electrochem. Soc.*, 2009, **156**, E187.
3 *Perovskite Oxide for Solid Oxide Fuel Cells*, ed. T. Ishihara, Springer, US, Boston, MA, 2009.
4 D. Karmakar, S. Datta and D. Jana, Combined theoretical and experimental study of the electronic and optical property of S_2WO_6, *J. Alloys Compd.*, 2021, **881**, 160586.
5 Y. Lu, H. Zhao, K. Li, X. Du, Y. Ma, X. Chang, N. Chen, K. Zheng and K. Świerczek, Effective calcium doping at the B-site of $BaFeO_{3-\delta}$ perovskite: towards low-cost and high-performance oxygen permeation membranes, *J. Mater. Chem. A*, 2017, **5**, 7999.
6 L. Wu, Y. Gao and J. Ma, Recent progress in multiferroic materials, *Sci. China: Technol. Sci.*, 2015, **58**, 2207.
7 J. Wang, Q. Liu, D. Xue and F. Li, Synthesis and characterization of $LaFeO_3$ nano particles, *J. Mater. Sci. Lett.*, 2002, **21**, 1059.
8 B. D. Cullity and S. R. Stock, *Elements of X-Ray Diffraction-Pearson Education Limited*, Pearson, Harlow, England, 3rd edn, 2014.
9 K. Dey, S. Sauerland, J. Werner, Y. Skourski, M. Abdel-Hafiez, R. Bag, S. Singh and R. Klingeler, Magnetic phase diagram and magnetoelastic coupling of $NiTiO_3$, *Phys. Rev. B*, 2020, **101**, 195122.
10 J. E. Silveira, A. S. De Souza, F. N. N. Pansini, A. R. Ribeiro, W. L. Scopel, J. A. Zazo, J. A. Casas and W. S. Paz, A comprehensive study of the reduction of nitrate on natural $FeTiO_3$: Photocatalysis and DFT calculations, *Sep. Purif. Technol.*, 2023, **306**, 122570.
11 R. A. P. Ribeiro, J. Andrés, E. Longo and S. R. Lazaro, Magnetism and multiferroic properties at $MnTiO_3$ surfaces: A DFT study, *Appl. Surf. Sci.*, 2018, **452**, 463.
12 M. Arruabarrena, A. Leonardo, M. Rodriguez-Vega, G. A. Fiete and A. Ayuela, Out-of-plane magnetic anisotropy in bulk ilmeniteCoTiO$_3$, *Phys. Rev. B*, 2022, **105**, 144425.
13 I. Piyanzina and R. Mamin, Toward the ferroelectric field-effect transistor on $BaTiO_3$/$LaMnO_3$ heterostructure: DFT investigation, *J. Mater. Sci.*, 2022, **57**, 21620.
14 D. Muñoz, N. M. Harrison and F. Illas, Electronic and magnetic structure ofLaMnO3from hybrid periodic density-functional theory, *Phys. Rev. B: Condens. Matter Mater. Phys.*, 2004, **69**, 085115.
15 M. Rizwan, A. Ali, Z. Usman, N. R. Khalid, H. B. Jin and C. B. Cao, Structural, electronic and optical properties of copper-doped $SrTiO_3$ perovskite: A DFT study, *Phys. B*, 2019, **552**, 52.
16 A. Ohtomo and H. Y. Hwang, A high-mobility electron gas at the $LaAlO_3$/$SrTiO_3$ heterointerface, *Nature*, 2004, **427**, 423.
17 M. K. Shahzad, S. Hussain, M. U. Farooq, A. Abdullah, G. A. Ashraf, M. Riaz and S. M. Ali, First principle investigation of tungsten based cubic oxide perovskite materials for superconducting applications: A DFT study, *J. Phys. Chem. Solids*, 2024, **186**, 111813.
18 M. A. Peña and J. L. G. Fierro, Chemical Structures and Performance of Perovskite Oxides, *Chem. Rev.*, 2001, **101**, 1981.
19 K. T. Butler, J. M. Frost and A. Walsh, Ferroelectric materials for solar energy conversion: photoferroics revisited, *Energy Environ. Sci.*, 2015, **8**, 838.
20 D. Peng, Y. Wang, H. Shi, W. Jiang, T. Jin, Z. Jin and Z. Chen, Fabrication of novel Cu_2WS_4/$NiTiO_3$ heterostructures for efficient visible-light photocatalytic hydrogen evolution and pollutant degradation, *J. Colloid Interface Sci.*, 2022, **613**, 194.
21 S. F. Matar, P. Mohn and G. Demazeau, The magnetic structure of $SrFeO_3$ calculated within LDA, *J. Magn. Magn. Mater.*, 1995, **140–144**, 169.
22 S. Tariq, A. O. Alrashdi, A. Al Bahir, S. M. S. Gilani, F. Hamioud, A. A. Mubarak, A. Ahmed and M. M. Saad H.-E, DFT insights into $LaFeO_3$ with Mn substitution: A promising path to energy-efficient magneto-optical applications, *J. Comput. Chem.*, 2024, **45**, 843.
23 M. Kumar, P. C. Sati, A. Kumar, M. Sahni, P. Negi, H. Singh, S. Chauhan and S. K. Chaurasia, Recent advances on magnetoelectric coupling in $BiFeO_3$: Technological achievements and challenges, *Mater. Today: Proc.*, 2022, **49**, 3046.
24 Y. Lu, H. Zhao, K. Li, X. Du, Y. Ma, X. Chang, N. Chen, K. Zheng and K. Świerczek, Effective Calcium Doping at the B-Site of BaFeO3−δ Perovskite: Towards Low-Cost and High-Performance Oxygen Permeation Membranes, *J. Mater. Chem. A*, 2017, **5**, 7999–8009.
25 R. Von Helmolt, J. Wecker, B. Holzapfel, L. Schultz and K. Samwer, Giant negative magnetoresistance in

perovskitelike$La_{2/3}Ba_{1/3}MnO_x$ ferromagnetic films, *Phys. Rev. Lett.*, 1993, **71**, 2331.
26 J. M. D. Coey, M. Viret and S. Von Molnár, Mixed-valence manganites, *Adv. Phys.*, 1999, **48**, 167.
27 T. Zhang, L. Liu, J. Hao, T. Zhu and G. Cui, Correlation analysis based multi-parameter optimization of the organic Rankine cycle for medium-and high-temperature waste heat recovery, *Appl. Therm. Eng.*, 2021, **188**, 116626.
28 Y. Lu, H. Zhao, K. Li, X. Du, Y. Ma, X. Chang, N. Chen, K. Zheng and K. Świerczek, Effective calcium doping at the B-site of $BaFeO_{3-\delta}$ perovskite: towards low-cost and high-performance oxygen permeation membranes, *J. Mater. Chem. A*, 2017, **5**, 7999.
29 A. Chesnokov, D. Gryaznov, E. A. Kotomin, J. Maier and R. Merkle, Protons in (Ga, Sc, In, Y) 3+-doped $BaFeO_3$ triple conductors—Site energies and migration barriers investigated by density functional theory calculations, *Solid State Ionics*, 2025, **421**, 116788.
30 I. V. Maznichenko, S. Ostanin, L. V. Bekenov, V. N. Antonov, I. Mertig and A. Ernst, Impact of oxygen doping and oxidation state of iron on the electronic and magnetic properties of $BaFeO_{3-\delta}$, *Phys. Rev. B*, 2016, **93**, 024411.
31 W. A. Adeagbo, I. V. Maznichenko, H. Ben Hamed, I. Mertig, A. Ernst and W. Hergert, Electronic and Magnetic Properties of $BaFeO_3$ on the Pt(111) Surface in a Quasicrystalline Approximant Structure, *Phys. Status Solidi B*, 2020, **257**, 1900649.
32 N. H. Hong, M. B. Kanoun, J.-G. Kim, T. S. Atabaev, K. Konishi, S. Noguchi, M. Kurisu and S. Goumri-Said, Shaping the Magnetic Properties of $BaFeO_3$ Perovskite-Type by Alkaline-Earth Doping, *J. Phys. Chem. C*, 2018, **122**(5), 2983–2989S.
33 C. Ononogbo, E. C. Nwosu, N. R. Nwakuba, G. N. Nwaji, O. C. Nwufo, O. C. Chukwuezie, M. M. Chukwu and E. E. Anyanwu, Opportunities of waste heat recovery from various sources: Review of technologies and implementation, *Heliyon*, 2023, **9**, e13590.
34 J. Wang, M. Saccoccio, D. Chen, Y. Gao, C. Chen and F. Ciucci, The effect of A-site and B-site substitution on $BaFeO_{3-\delta}$: An investigation as a cathode material for intermediate-temperature solid oxide fuel cells, *J. Power Sources*, 2015, **297**, 511.
35 H. J. Kim, *et al.*, High Mobility in a Stable Transparent Perovskite Oxide, *Appl. Phys. Express*, 2012, **5**, 061102.
36 H. J. Kim, *et al.*, Physical properties of transparent perovskite oxides (Ba,La)SnO_3 with high electrical mobility at room temperature, *Phys. Rev. B: Condens. Matter Mater. Phys.*, 2012, **86**, 165205.
37 B. Das, I. Aguilera, U. Rau and T. Kirchartz, Effect of Doping, Photodoping, and Bandgap Variation on the Performance of Perovskite Solar Cells, *Adv. Opt. Mater.*, 2022, **10**, 2101947.
38 H. Van Ngoc and H. T. P. Thuy, Group I elements-adsorbed NiZnO monolayer: Electro-optical properties and potential applications, *Phys. B*, 2025, **700**, 416922.
39 H. Ali, *et al.*, Defect-driven innovations in photocatalysts: Pathways to enhanced photocatalytic applications, *InfoMat*, 2025, e70040.
40 H. Tong, *et al.*, Interface Engineering, Charge Carrier Dynamics, and Solar-Driven Applications of Halide Perovskite/2D Material Heterostructured Photocatalysts, *ACS Appl. Mater. Interfaces*, 2025, **17**, 23431.
41 P. Sen, P. Bhattacharya, G. Mukherjee, J. Ganguly, B. Marik, D. Thapliyal, S. Verma, G. D. Verros, M. S. Chauhan and R. K. Arya, Advancements in Doping Strategies for Enhanced Photocatalysts and Adsorbents in Environmental Remediation, *Technologies*, 2023, **11**, 144.
42 M. M. V. Petrović, J. D. Bobić, T. Ramoška, J. Banys and B. D. Stojanović, Antimony doping effect on barium titanate structure and electrical properties, *Ceram. Int.*, 2011, **37**, 2669.
43 F. Kang, L. Zhang, L. He, Q. Sun, Z. Wang, R. Kang, P. Mao, C. Zhu and J. Wang, Enhanced electric field induced strain in B-site Sb doped $BiFeO_3$-$BaTiO_3$ lead free ceramics, *J. Alloys Compd.*, 2021, **864**, 158917.
44 C. Sun, J. A. Alonso and J. Bian, Recent Advances in Perovskite-Type Oxides for Energy Conversion and Storage Applications, *Adv. Energy Mater.*, 2021, **11**, 2000459.
45 M. H. A. Mhareb, E. Hannachi, Y. Slimani, M. I. Sayyed, N. Dwaikat, M. K. Hamad, Y. S. Alajerami, M. A. Almessiere and A. Baykal, Radiation shielding and structural features for different perovskites doped $YBa_2Cu_3O_y$ composites, *Ceram. Int.*, 2022, **48**, 18855.
46 A. Iio, H. Ikeda, S. A. Anggraini and N. Miura, Potentiometric YSZ-based oxygen sensor using BaFeO3 sensing-electrode, *Electrochem. Commun.*, 2014, **48**, 134.
47 P. Blaha, K. Schwarz, F. Tran, R. Laskowski, G. K. H. Madsen and L. D. Marks, WIEN2k: An APW+lo program for calculating the properties of solids, *J. Chem. Phys.*, 2020, **152**, 074101.
48 P. Blaha, K. Schwarz, P. Sorantin and S. B. Trickey, Full-potential, linearized augmented plane wave programs for crystalline systems, *Comput. Phys. Commun.*, 1990, **59**, 399.
49 K. Schwarz and P. Blaha, Solid state calculations using WIEN2k, *Comput. Mater. Sci.*, 2003, **28**, 259.
50 J. P. Perdew, K. Burke and Y. Wang, Generalized gradient approximation for the exchange-correlation hole of a many-electron system, *Phys. Rev. B: Condens. Matter Mater. Phys.*, 1996, **54**, 16533.
51 H. J. Kulik, Perspective: Treating electron over-delocalization with the DFT+U method, *J. Chem. Phys.*, 2015, **142**, 240901.
52 H. J. Monkhorst and J. D. Pack, Special points for Brillouin-zone integrations, *Phys. Rev. B*, 1976, **13**, 5188.
53 M. Dressel and G. Grüner, *Electrodynamics of Solids: Optical Properties of Electrons in Matter*, Cambridge University Press, Cambridge; New York, 2002.
54 G. K. Madsen, J. Carrete and M. J. Verstraete, BoltzTraP2, a program for interpolating band structures and calculating semi-classical transport coefficients, *Comput. Phys. Commun.*, 2018, **231**, 140.

55 A. Kokalj, XCrySDen—a new program for displaying crystalline structures and electron densities, *J. Mol. Graphics Modell.*, 1999, **17**, 176.
56 N. Hayashi, T. Yamamoto, H. Kageyama, M. Nishi, Y. Watanabe, T. Kawakami, Y. Matsushita, A. Fujimori and M. Takano, $BaFeO_3$: A Ferromagnetic Iron Oxide, *Angew. Chem.*, 2011, **123**, 12755.
57 I. Cherair, N. Iles, L. Rabahi and A. Kellou, Effects of Fe substitution by Nb on physical properties of $BaFeO_3$: A DFT+U study, *Comput. Mater. Sci.*, 2017, **126**, 491.
58 W. W. Malinofsky and H. Kedesdy, Barium Iron Oxide Isomorphs of Hexagonal and Tetragonal $BaTiO_3$, *J. Am. Chem. Soc.*, 1954, **76**, 3090.
59 S. C. Tidrow, Mapping Comparison of Goldschmidt's Tolerance Factor with Perovskite Structural Conditions, *Ferroelectrics*, 2014, **470**, 13.
60 A. Kumar, A. S. Verma and S. R. Bhardwaj, Prediction of Formability in Perovskite-Type Oxides∼!2008-08-05∼!2008-10-08∼!2008-12-05, *Open Appl. Phys. J.*, 2008, **1**, 11.
61 R. D. Shannon, Revised effective ionic radii and systematic studies of interatomic distances in halides and chalcogenides, *Found. Crystallogr.*, 1976, **32**, 751.
62 T. Kida, D. Takauchi, K. Watanabe, M. Yuasa, K. Shimanoe, Y. Teraoka and N. Yamazoe, Oxygen Permeation Properties of Partially A-Site Substituted $BaFeO_{3-\delta}$ Perovskites, *J. Electrochem. Soc.*, 2009, **156**, E187.
63 K. Zakharchuk, A. Kovalevsky and A. Yaremchenko, Synthesis and characterization of $Ba(Fe,Zr,Ni)O_{3-\delta}$ perovskites for potential electrochemical applications, *J. Alloys Compd.*, 2023, **956**, 170250.
64 C. Li, K. C. K. Soh and P. Wu, Formability of ABO_3 perovskites, *J. Alloys Compd.*, 2004, **372**, 40.
65 D. Ji, S. Feng, L. Wang, S. Wang, M. Na, H. Zhang, C. Zhang and X. Li, Regulatory tolerance and octahedral factors by using vacancy in APbI3 perovskites, *Vacuum*, 2019, **164**, 186.
66 N. Hayashi, T. Yamamoto, H. Kageyama, M. Nishi, Y. Watanabe, T. Kawakami, Y. Matsushita, A. Fujimori and M. Takano, $BaFeO_3$: A Ferromagnetic Iron Oxide, *Angew. Chem., Int. Ed.*, 2011, **50**, 12547.
67 M. F. Hoedl, D. Gryaznov, R. Merkle, E. A. Kotomin and J. Maier, Interdependence of Oxygenation and Hydration in Mixed-Conducting $(Ba,Sr)FeO_{3-\delta}$ Perovskites Studied by Density Functional Theory, *J. Phys. Chem. C*, 2020, **124**, 11780.
68 S. V. Faleev and F. Léonard, Theory of enhancement of thermoelectric properties of materials with nanoinclusions, *Phys. Rev. B: Condens. Matter Mater. Phys.*, 2008, **77**, 214304.
69 J. M. Coey, *Magnetism and Magnetic Materials*, Cambridge university press, 2010.
70 H. J. Cho, K. Sato, M. Wei, G. Kim and H. Ohta, Effect of lattice distortions on the electron and thermal transport properties of transparent oxide semiconductor Ba1-xSrxSnO3 solid solution films, *J. Appl. Phys.*, 2020, **127**, 115701.
71 H. Gleiter, Nanocrystalline materials, *Prog. Mater. Sci.*, 1989, **33**, 223.
72 T. Uesugi and K. Higashi, First-principles studies on lattice constants and local lattice distortions in solid solution aluminum alloys, *Comput. Mater. Sci.*, 2013, **67**, 1.
73 G. Rahman and S. Sarwar, Ground State Structure of $BaFeO_3$: Density Functional Theory Calculations, *arXiv*, 2017, preprint, arXiv:1604.06040, DOI: **10.1007/s10948-017-4223-1**.
74 M. F. Hoedl, C. Ertural, R. Merkle, R. Dronskowski and J. Maier, The Orbital Nature of Electron Holes in $BaFeO_3$ and Implications for Defect Chemistry, *J. Phys. Chem. C*, 2022, **126**, 12809.
75 C. Kittel, *Int. to Solid State Physics*, Maruzen, 8th edn, 2005.
76 U. S. Shenoy, B. Amin and D. K. Bhat, Exploring the impact of modulation of electronic structure via doping in the realm of environmental applications, *NanoTrends*, 2025, **9**, 100075.
77 H.-J. Feng and F.-M. Liu, Electronic Structure of $BaFeO_3$: An Abinitio DFT Study, *arXiv*, 2007, preprint, arXiv:0704.2985, DOI: **10.48550/arXiv.0704.2985**.
78 H. M. Christen and G. Eres, Recent advances in pulsed-laser deposition of complex oxides, *J. Phys.: Condens. Matter*, 2008, **20**, 264005.
79 H. V. Ngoc and H. T. P. Thuy, Investigation of Be, Mg, Ti–adsorbed boron-germanene nanoribbons for nano applications, *J. Phys.: Condens. Matter*, 2024, **36**, 505901.
80 A. E. Bocquet, T. Mizokawa, T. Saitoh, H. Namatame and A. Fujimori, Electronic structure of 3d-transition-metal compounds by analysis of the 2p core-level photoemission spectra, *Phys. Rev. B: Condens. Matter Mater. Phys.*, 1992, **46**, 3771.
81 C. Callender, D. P. Norton, R. Das, A. F. Hebard and J. D. Budai, Ferromagnetism in pseudocubic $BaFeO_3$ epitaxial films, *Appl. Phys. Lett.*, 2008, **92**, 012514.
82 M. Hussain, F. Ali, H. Ullah, S. T. Iqbal, Y.-H. Shin, F. Anjum and E. A. Al-Ammar, Doping dependent magnetic and thermoelectric response of perovskite $BaGeO_3$ for spintronics and energy applications, *Comput. Condens. Matter.*, 2024, **41**, e00973.
83 Y. Bai, Y. Fang, Y. Deng, Q. Wang, J. Zhao, X. Zheng, Y. Zhang and J. Huang, Low Temperature Solution-Processed $Sb:SnO_2$ Nanocrystals for Efficient Planar Perovskite Solar Cells, *ChemSusChem*, 2016, **9**, 2686.
84 J. Gebhardt and A. M. Rappe, Doping of $BiFeO_3$: A comprehensive study on substitutional doping, *Phys. Rev. B*, 2018, **98**, 125202.
85 C. C. Homes, S. Khim and A. P. Mackenzie, Perfect separation of intraband and interband excitations in PdCoO2, *Phys. Rev. B*, 2019, **99**, 195127.
86 J. A. Majewski and P. Vogl, Simple model for structural properties and crystal stability of sp-bonded solids, *Phys. Rev. B: Condens. Matter Mater. Phys.*, 1987, **35**, 9666.
87 M. B. Hossain Parosh, M. Saiduzzaman, J. Islam, N. Jahan Nisha and I. Ahmed Ovi, A first-principles study of dynamically stable non-toxic photovoltaic Mg_3PX_3(X = Cl and Br) compounds, *RSC Adv.*, 2025, **15**, 10085.
88 M. S. Islam, M. F. Rahman, M. R. Islam, A. Ghosh, M. A. Monnaf, M. S. Reza, M. K. Hossain, A. Zaman,

S. Ezzine and L. Ben Farhat, An in-depth analysis of how strain impacts the electronic, optical, and output performance of the Ca3NI3 novel inorganic halide perovskite, *J. Phys. Chem. Solids*, 2024, **185**, 111791.

89 J. Sun, X.-F. Zhou, Y.-X. Fan, J. Chen, H.-T. Wang, X. Guo, J. He and Y. Tian, First-principles study of electronic structure and optical properties of heterodiamond BC_2N, *Phys. Rev. B: Condens. Matter Mater. Phys.*, 2006, **73**, 045108.

90 F. Parvin, M. A. Hossain, M. S. Ali and A. Islam, Mechanical, electronic, optical, thermodynamic properties and superconductivity of $ScGa_3$, *Phys. B*, 2015, **457**, 320.

91 S. Huang, R.-Z. Li, S.-T. Qi, B. Chen and J. Shen, A theoretical study of the elastic and thermal properties of ScRu compound under pressure, *Phys. Scr.*, 2014, **89**, 065702.

92 F. Wooten, *Optical Properties of Solids*, Academic Press, 1972.

93 M. Fox, *Optical Properties of Solids*, Oxford university press, 2010, vol. 3.

94 M. Dressel and G. Grüner, *Electrodynamics of Solids: Optical Properties of Electrons in Matter*, Cambridge university press, 2002.

95 I. Cherair, N. Iles, L. Rabahi and A. Kellou, Effects of Fe substitution by Nb on physical properties of $BaFeO_3$: A DFT+U study, *Comput. Mater. Sci.*, 2017, **126**, 491.

96 I. V. Maznichenko, S. Ostanin, L. V. Bekenov, V. N. Antonov, I. Mertig and A. Ernst, Impact of oxygen doping and oxidation state of iron on the electronic and magnetic properties of $BaFeO_{3-\delta}$, *Phys. Rev. B*, 2016, **93**, 024411.

97 T. He and R. J. Cava, Disorder-induced ferromagnetism in $CaRuO_3$, *Phys. Rev. B: Condens. Matter Mater. Phys.*, 2001, **63**, 172403.

98 A. Ghosh, D. P. Trujillo, H. Choi, S. M. Nakhmanson, S. P. Alpay and J.-X. Zhu, Electronic and Magnetic Properties of Lanthanum and Strontium Doped Bismuth Ferrite: A First-Principles Study, *Sci. Rep.*, 2019, **9**, 194.

99 G. Pizzi, D. Volja, B. Kozinsky, M. Fornari and N. Marzari, BoltzWann: A code for the evaluation of thermoelectric and electronic transport properties with a maximally-localized Wannier functions basis, *Comput. Phys. Commun.*, 2014, **185**, 422.

100 G. J. Snyder and E. S. Toberer, Complex thermoelectric materials, *Nat. Mater.*, 2008, **7**, 105.

101 M. R. Shankar and A. N. Prabhu, A review on structural characteristics and thermoelectric properties of mid-temperature range Chalcogenide-based thermoelectric materials, *J. Mater. Sci.*, 2023, **58**, 16591.

102 X. Song, G. Wang, L. Zhou, H. Yang, X. Li, H. Yang, Y. Shen, G. Xu, Y. Luo and N. Wang, Oxide Perovskite $BaSnO_3$: A Promising High-Temperature Thermoelectric Material for Transparent Conducting Oxides, *ACS Appl. Energy Mater.*, 2023, DOI: **10.1021/acsaem.3c01870**.